Provided for non-commercial research and education use.
Not for reproduction, distribution or commercial use.

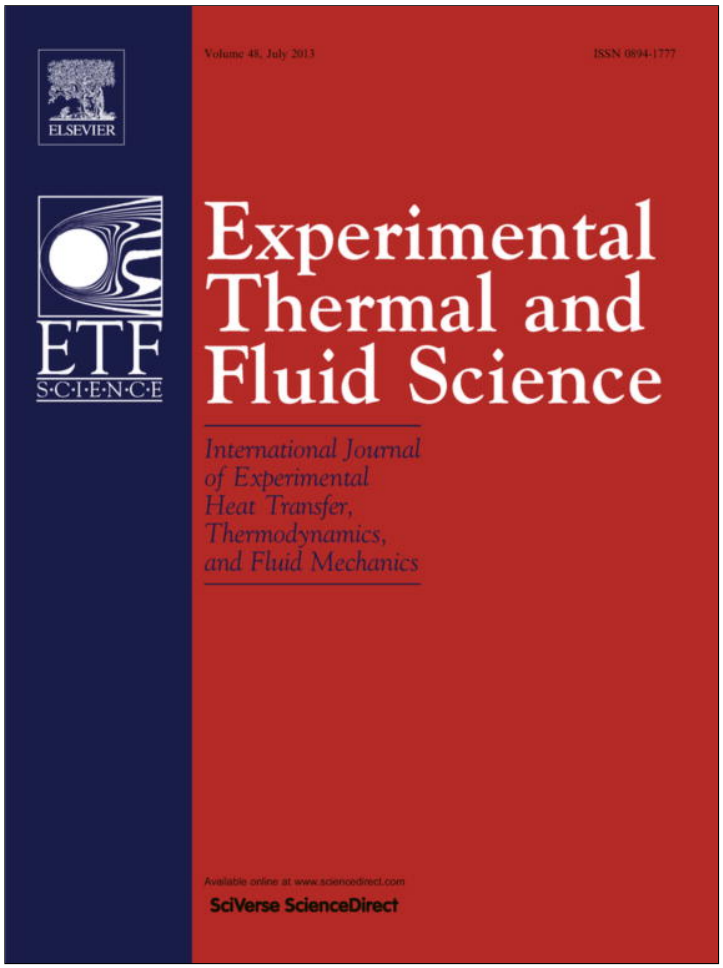

This article appeared in a journal published by Elsevier. The attached copy is furnished to the author for internal non-commercial research and education use, including for instruction at the authors institution and sharing with colleagues.

Other uses, including reproduction and distribution, or selling or licensing copies, or posting to personal, institutional or third party websites are prohibited.

In most cases authors are permitted to post their version of the article (e.g. in Word or Tex form) to their personal website or institutional repository. Authors requiring further information regarding Elsevier's archiving and manuscript policies are encouraged to visit:

http://www.elsevier.com/authorsrights

Author's personal copy

Experimental Thermal and Fluid Science 48 (2013) 198–212

Contents lists available at SciVerse ScienceDirect

Experimental Thermal and Fluid Science

journal homepage: www.elsevier.com/locate/etfs

Pool boiling heat transfer on uniform and non-uniform porous coating surfaces

Xianbing Ji [a,b], Jinliang Xu [a,c,*], Ziwei Zhao [b,c], Wolong Yang [c]

[a] State Key Laboratory of Alternate Electrical Power System with Renewable Energy Sources, North China Electric Power University, Beijing 102206, PR China
[b] The Beijing Key Laboratory of Multiphase Flow and Heat Transfer, North China Electric Power University, Beijing 102206, PR China
[c] The Beijing Key Laboratory of Energy Safety and Clean Utilization, North China Electric Power University, Beijing 102206, PR China

ARTICLE INFO

Article history:
Received 8 November 2012
Received in revised form 11 February 2013
Accepted 3 March 2013
Available online 14 March 2013

Keywords:
Pool boiling
Porous heater surface
Critical heat flux
Boiling pattern

ABSTRACT

Pool boiling heat transfer experiments were performed using acetone as the working fluid at atmospheric pressure on seven heater surfaces, which can be divided into three types. The first, second and third types refer to the plain surface with poor heat transfer, the open channel surface and uniform porous coating surface with moderate heat transfer enhancement, and the 2-D/3-D porous coating surfaces with significant heat transfer enhancement. The open channel surface and uniform porous coating surface had intercrossed boiling curves, with better performance for the uniform porous coating surface due to the enhanced nucleation heat transfer at small or moderate wall superheats, and better performance for the open channel surface at large wall superheats due to the vapor channel provided. The 2-D porous coating surface with the pitch width of 1.6 mm yields the best heat transfer performance and the largest critical heat fluxes among the three 2-D surfaces. The 3-D porous coating surface (TS#7) significantly increases the critical heat flux, which can be 3.7 times of that for the plain surface. Boiling curves were shifted to smaller wall superheat region and critical heat fluxes were increased with increases in liquid subcoolings. Two distinct bubble patterns existed for 2-D/3-D porous coating surfaces: continuously-isolated-bubble-escape pattern at small or moderate heat fluxes, and periodically-large-bubble-escape pattern at large heat fluxes. The hollow well at the heater center and/or the porous stacks exposed in liquid are acted as the liquid supply duct at high heat fluxes. This explains the reason that the porous coating surfaces with periodically varied particle layer thicknesses had larger critical heat fluxes than other heater surfaces.

© 2013 Elsevier Inc. All rights reserved.

1. Introduction

Pool boiling is a well-recognized means for passively removing high heat loads from a heater surface while maintains relatively low material temperatures. Various surface modifications, including integrated surface structures (e.g. channels and fins) and utilization of a uniform porous coating on the heater surface, have shown to effectively enhance the pool boiling heat transfer [1–3]. The enhancement is attributed to the combinations of the following effects: an extended surface area effect, an increased nucleation site effect, a capillary assisted liquid supply towards the heater surface effect, and the vapor escape from the porous-layer to the pool liquid effect [4]. These effects are dependent on the solid and liquid thermophysical properties and porous parameters such as porosity, pore size, its distribution and porous-layer thickness. The exact relationship among these effects is not known yet.

In a general sense, the pool boiling heat transfer on plain and porous coating surface involves the counterflow of vapor release and liquid supply. Considering boiling heat transfer on a uniform porous-layer coating surface, the liquid supply is strongly related to the capillary pressure written as $\Delta p = 4\sigma/d_p$. Here σ is the surface tension and d_p is the pore diameter. A small pore size yields a large capillary pressure to result in a large liquid supply capability. Now we turn to consider the vapor release into the pool liquid. Meléndez and Reyes [5] gave the vapor mass flow rate from the porous media as

$$m = \frac{\pi}{128}\left(\frac{\rho_v \sigma}{\mu_v}\right)\left(\frac{\varepsilon d_p^3}{\delta}\right) \tag{1}$$

where ρ_v and μ_v are the vapor density and viscosity respectively, ε is the porous porosity, δ is the porous thickness. It is seen from Eq. (1) that a larger pore size achieves a larger vapor mass flow rate.

The above analysis gave the strong indication that the liquid supply and vapor release require different pore sizes. A small pore size is helpful for the liquid supply towards the phase change surface but hinders the vapor escape into the pool liquid. When heat

* Corresponding author at: State Key Laboratory of Alternate Electrical Power System with Renewable Energy Sources, North China Electric Power University, Beijing 102206, PR China. Tel.: +86 10 61772268.
E-mail address: xjl@ncepu.edu.cn (J. Xu).

0894-1777/$ - see front matter © 2013 Elsevier Inc. All rights reserved.
http://dx.doi.org/10.1016/j.expthermflusci.2013.03.002

Author's personal copy

Nomenclature

A	area (m^2)
a_0 and a_1	empirically determined constants for temperature distribution in copper block
C_{pl}	specific heat of saturated liquid (J/kg K)
C_{pv}	specific heat of saturated vapor (J/kg K)
d_p	pore diameter (m)
g	gravity acceleration (m/s^2)
h	heat transfer coefficient with foam structure (W/m^2 K)
h_{lv}	latent heat of evaporation (J/kg)
k_s	thermal conductivity of solid copper (W/m K)
m	mass flux of vapor phase (kg/m^2 s)
Δp	capillary pressure (Pa)
q	heat flux (W/m^2)
q_{CHF}	critical heat flux (W/m^2)
R	base radius (m)
T	temperature (K or °C)
ΔT_{sat}	wall superheat (K or °C)
$\frac{dT}{dz}\Big\|_{\text{base surface}}$	temperature gradient at the base surface (K/m)
t	time (s)
w	pitch width (m)
z	coordinate perpendicular to the base surface m

Greek symbols

δ	porous coating thickness (m)
ε	porosity of porous coating
λ_b	length scale
λ_m	wavelength (m)
μ	viscosity (kg/m s)
ρ	density (kg/m^3)
σ	surface tension (N/m)

Subscripts

b	base of porous surface
$bulk$	pool bulk condition
l	liquid phase
s	solid
sat	saturation condition
v	vapor phase
w	wall surface condition

flux is increased, the generated vapor may be trapped within the porous pores to yield the hot spot dryout [6]. On the other hand, a large pore size possesses small flow resistance of the vapor release into the pool liquid, but the liquid supply towards the phase change surface may be insufficient at high heat fluxes, under which critical heat flux (CHF) encounters.

Multiscale porous surfaces are surfaces with varied particle layer thicknesses. The modulation is imposed to generate alternating regions of low resistance to vapor escape and high capillary-assisted liquid draw [7]. The multiscale porous surface consists of periodical porous stacks and valleys. The liquid suction is fulfilled within the pores of porous stacks, and vapor is released via the valley. The periodically arranged porous stacks satisfy the requirements of large valley size for vapor escape and small pore size for liquid suction. The modulation separates the flow paths of liquid and vapor phases to decrease the counterflow resistance adjacent to the surface.

Theories were proposed by Liter and Kaviany [8] for two independent mechanisms capable of causing the liquid choking that leads to CHF. The Zuber's hydrodynamic theory was modified to consider the coating modulation-wavelength on the vapor layer development above the coating surface, which effectively hinders the liquid downflow towards the coatings. The second liquid-choking limit occurs when the viscous drag suppresses the capillary pumping capability. The lower of liquid choking limits is theorized to predict the CHF.

Min et al. [9] developed a new fabrication method to readily make 2-D and 3-D modulated coatings for enhanced pool boiling performance. The coated stacks had different height, width, and pitch (modulation wavelength), particle diameter and porosity. The 2-D and 3-D coatings were found to have similar CHFs, indicating the strong effect of modulation wavelength and weak effect of particle size and porosity.

The separation of flow paths of liquid and vapor phases can also be fulfilled using the biporous wicks. Semenic and Catton [10] investigated biporous wicks, having two distinguished characteristic pore sizes. For comparison, monoporous wicks had a single characteristic pore size. Thin biporous wicks reached higher CHFs than monoporous wicks because they develop the evaporating menisci not only on the top of the wick surface but also inside the wick. Thick biporous wicks had better performance on CHFs than thin biporous wicks. This is possible because liquid can be supplied at the top layer of the wick towards the evaporating menisci above the vapor blanket region.

Recent, Lin et al. [11] developed an evaporative heat transfer model for a loop heat pipe with biporous wick structure. The effect of wick pore size distribution on heat transfer was considered. The evaporator wick was assumed to have three regions at the heating condition: a vapor blanket, a two-phase region and a saturated liquid region. The evaporator wall temperature and the total thermal resistance at different heat loads were predicted with ammonia as the working fluid. The predictions showed distinct heat transfer characteristics and higher performance for the bidisperse wick compared to monoporous wick. A bidisperse wick decreases the vapor blanket thickness, which behaves a thermal resistance and causes lower heat transfer capacity of the evaporator.

We investigated the pool boiling heat transfer of acetone at atmosphere pressure. The objective of this paper is to examine the effects of porous structure for liquid suction and valley channel for vapor escape. In order to do so, we prepared seven heater surfaces, including the reference plain surface, thick porous coating surface with uniform particle layer thickness, and 2-D and 3-D porous coating surfaces with periodically varied particle layer thicknesses. The boiling curves, heat transfer coefficients and boiling patterns were obtained. It is found that the 2-D and 3-D porous surfaces significantly enhance the pool boiling heat transfer. The temporarily existed hollow well at the heater center and exposed porous stacks in liquid are the reason for the non-uniform porous surfaces to have significantly large critical heat fluxes.

2. The heater surfaces and experimental setup

2.1. The heater surfaces with and without porous coatings

Table 1 shows the seven heater surfaces, which were made with copper substrate and can be divided into four types: (1) the 2000 mesh sandpaper polished plain surface (TS#1); (2) open channel surface with w (pitch width) = 1.0 mm and δ (fin height) = 2.5 mm (TS#2); (3) uniform porous coating surface (TS#3, δ = 2.5 mm, ε = 0.32 and d_p = 130–170 μm); (4) 2-D and 3-D porous coating surfaces (TS#4–7). We Note that d_p is the particle diameter.

TS#2 was a machined groove-channel surface without particles sintered and polished by 2000 mesh sandpaper after its fabrication.

Author's personal copy

Table 1
Heater surfaces used in this study.

Heater surface	Name	Configuration	Parameters
TS#1	Plain surface	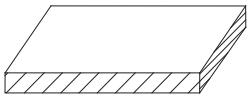	
TS#2	Microchannel surface	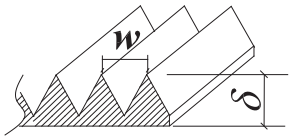	w = 1.0 mm, δ = 2.5 mm
TS#3	Uniform porous coating surface	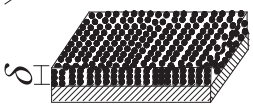	δ = 2.5 mm, ε = 0.32, d_p = 130–170 μm
TS#4 TS#5 TS#6	2-D porous coating surface	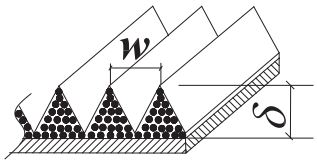	w = 1.0 mm, δ = 2.5 mm, ε = 0.3 2, d_p = 130–170 μm w = 1.6 mm; δ = 2.5 mm, ε = 0.3 2, d_p = 130–170 μm w = 2.0 mm; δ = 2.5 mm, ε = 0.32, d_p = 130–170 μm
TS#7	3-D porous coating surface		w = 2.0 mm; δ = 2.5 mm, ε = 0.3 2, d_p = 130–170 μm

Note: TS means test surface.

The use of this surface was for comparison purpose. Thus the SEM image file for TS#2 was not provided. Fig. 1 gave the SEM pictures for 2-D and 3-D porous coating surfaces, having the porosity of 0.32 and particle diameter of 130–170 μm. TS#3 had a uniform porous coating thickness of 2.5 mm (see Fig. 1a). Three pitch widths were prepared to yield three 2-D porous coating surfaces, with w = 1.0 mm for TS#4, w = 1.6 mm for TS#5 and w = 2.0 mm for TS#6. Other parameters except w were identical for TS#4–6. TS#7 was the 3-D porous coating surface with w = 2.0 mm. In the modified Zuber's hydrodynamic stability theory, the pitch width was assumed to be the modulation wavelength [12].

The porous coating thickness is an important parameter to influence the pool boiling heat transfer. Min et al. [9] used the thickness in the range of 0.7–2.0 mm for the 2-D and 3-D modulated porous coatings to enhance the pool boiling heat transfer. Semenic and Catton [10] used the porous coating thicknesses of 0.8–3.0 mm and noted that thick biporous wicks could reach higher CHF than thin biporous wicks because they continue to operate although the vapor blanket (film boiling) exists on the heated surface. This is possible because the top layer of the wick continues to supply liquid to the evaporating menisci above the vapor blanket region and vapor jets form between large pores of the wick and vent the vapor out of the wick. It was also found that for thick biporous wicks operating at very high heat fluxes, the heat conducts radially into the wick. We used the porous coating thickness of 2.5 mm in this study.

We note that there was a particle substrate with its layer thickness of about 0.5 mm for 2-D and 3-D porous coating surfaces. Thus the 2-D and 3-D porous stacks had the height of about 2.0 mm. Fig. 1 shows that 2-D porous coating surfaces had 2-D porous stacks for liquid suction and valley grooves for vapor release. The 3-D porous coating surface had periodically arranged conical stacks for liquid suction and valley part for vapor release. The multicsale porous surfaces smartly apply the flow path separation concept. The liquid downflow towards the evaporating menisci was completed via the 2-D/3-D porous stacks while vapor was escaping through the valley part of the configuration (see Fig. 2).

2.2. The experimental setup

Fig. 3 shows the copper block test section. Five cartridge heaters were inserted in 6.0 mm diameter holes at the copper block bottom, providing heating power to the copper block. Each cartridge heater had a maximum power of 100 W at an AC voltage of 220 V. The middle part of the copper block had three 1.0 mm diameter holes. Three K-type thermocouples were inserted in the miniature holes.

The top of the copper block was a rectangular plate with a thickness of 3.0 mm. The sand polished copper surface was treated as the reference surface (called TS#1 in Table 1). The plate surface area was 12.0 mm by 12.0 mm. The TS#2 surface was an open channel surface. The microchannels were directly machined on the top of the copper block. TS#3–7 are 2-D and 3-D porous coating surfaces, which were sintered on the top of the copper block with periodically varied thicknesses of the deposition layer.

Fig. 4 illustrates the experimental setup. The test heater surface and liquid were enclosed in a transparent glass chamber. The bottom of the glass chamber was a stainless steel plate. A rectangular hole was at the center of the stainless steel plate to fit the copper block. Teflon was adapted between the stainless steel plate and copper block. Epoxy glue was filled for seal. There was no liquid leakage for such hardware arrangement. The heater surface was immersed in the pool liquid. The main body of the copper block outside of the glass chamber was insulated by the thermal insulation material.

During the boiling experiment, the glass chamber was kept at the atmospheric pressure. Fig. 4 also shows the power supply system, consisting of a 220 V voltage stabilizer, a voltage transformer

Author's personal copy

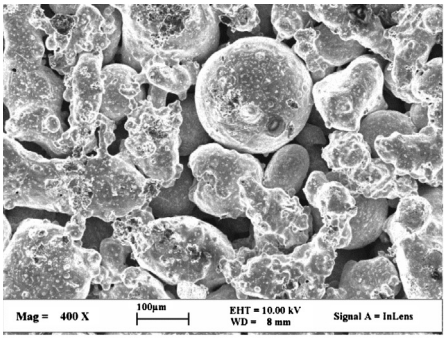

(a) SEM image for TS#3

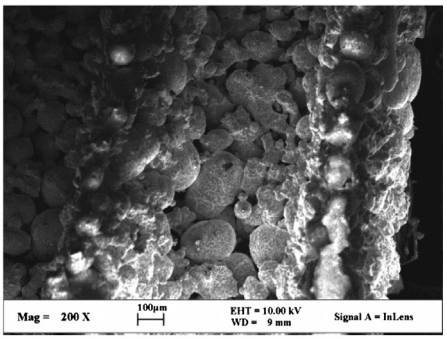

(b) SEM image for TS#4

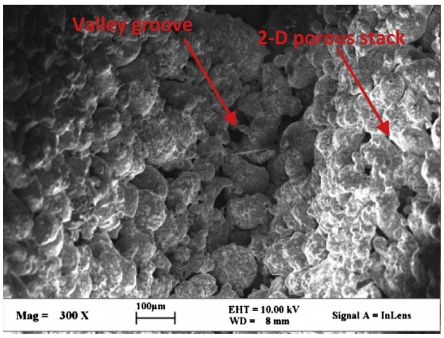

(c) SEM image for TS#5

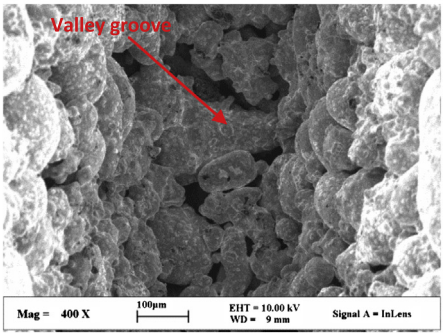

(d) SEM image for TS#6

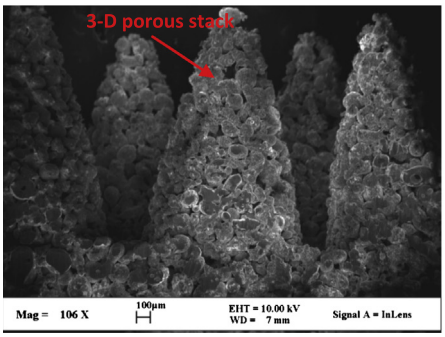

(e) SEM image for TS#7

Fig. 1. The SEM photos for uniform and non-uniform porous coating surfaces.

and a powermeter. The powermeter gave the power reading. All the temperature signals were recorded by a Hewlett–Packard data acquisition system. A high speed camera collected the boiling patterns with millisecond time scale.

The pool liquid temperature should be well controlled during the experiment. This can be fulfilled by a vapor condenser out of the glass chamber (component 1 in Fig. 4), a cooper coiled tube with tap water flowing inside and an auxiliary heater in the glass chamber (components 2 and 3 in Fig. 4). The pool liquid temperature was measured by a jacket thermocouple. The major heat was dissipated to the environment by the vapor condenser. The copper coiled tube and the auxiliary heater precisely modulate the pool liquid temperature with an uncertainty of 0.5 °C. The experiment procedures are as follows:

- Charge acetone in the glass chamber and turn on the cartridge heaters to vigorously boil the liquid for our hour to remove the condensable gas in liquid and porous structure.
- The formal experiment starts from a small heat flux on the heater surface such as $q = 1$ W/cm^2.
- Setup a desired pool liquid temperature.
- If the measured pool liquid temperature was smaller than the desired value, the auxiliary heater was automatically turned on until the desired temperature was reached.
- Alternatively, if the measured pool liquid temperature was higher than the desired value, the auxiliary heater was automatically turned off while the tap water flow rate was manually adjusted until the desired temperature was reached.
- Collect the data when the system was operating stably.
- Increase the heat flux on the heater surface and repeat the above procedures.
- The experiment was stopped until the critical heat flux was reached.

2.3. The data reduction

One-dimensional thermal conduction heat transfer within the middle part containing T_1, T_2 and T_3 (see Fig. 3) was assumed. Such assumption was also used in Ref. [13]. The heat flux was defined as $q = -k_s \frac{dT}{dz}\big|_{\text{base surface}}$, where k_s is the copper thermal conductivity, $\frac{dT}{dz}\big|_{\text{base surface}}$ is the temperature gradient at the base surface below the sintered particle layer, z is the coordinate perpendicular to

Author's personal copy

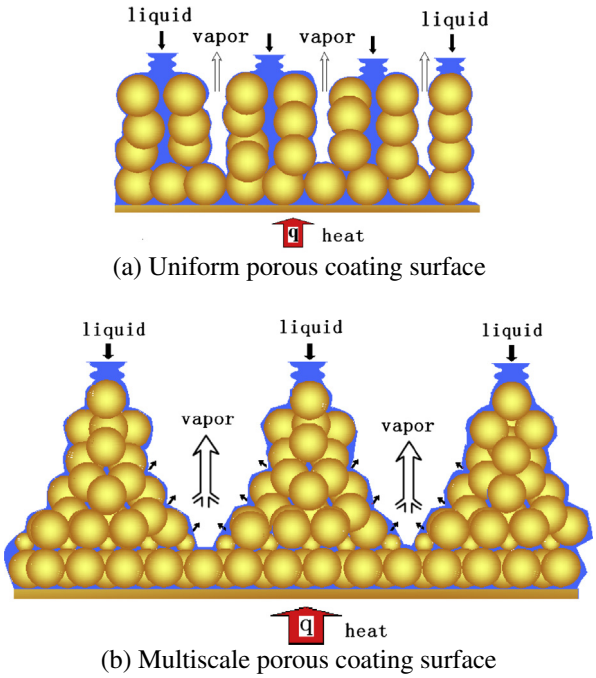

Fig. 2. The principle for liquid suction and vapor release with different scales.

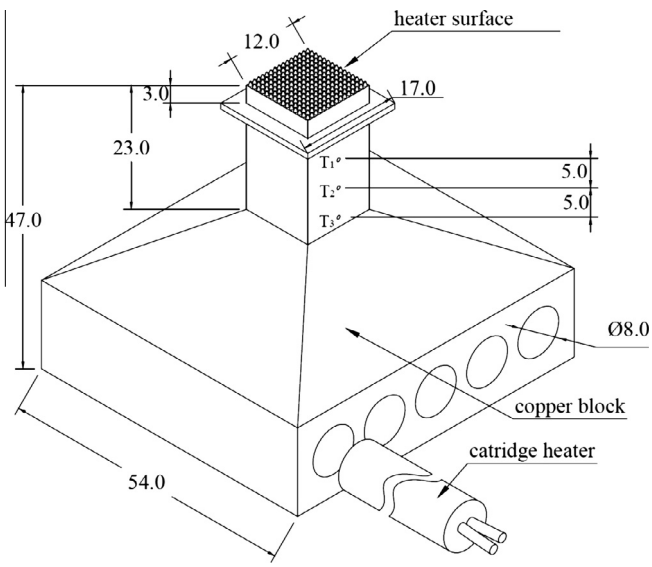

Fig. 3. The heating block (all dimensions are in mm).

the base surface. A least square correlation of temperatures versus z was written as $T = a_0 + a_1 z$, where a_0, and a_1 are constants correlated based on T_1, T_2, and T_3 (see Fig. 3). The heat flux uncertainty was estimated to be smaller than 6.0%. The surface superheat ΔT_{sat} was defined as the surface temperature (T_w) subtracting T_{sat}, where T_w is the temperature at the base surface, T_{sat} is the saturation temperature of acetone at atmospheric pressure. Heat transfer coefficient was calculated as

$$h = q/(T_w - T_{bulk}) \tag{2}$$

where T_{bulk} is the pool liquid temperature. The surface temperature, surface superheat, and pool liquid temperature had the maximum uncertainties of 0.3 °C.

We estimated the uncertainty of the heat transfer coefficient, which is a function of three independent parameters of q, T_w and T_{bulk}. The uncertainty of h was calculated as

$$\Delta h = \sqrt{\left(\frac{\partial h}{\partial q}\right)^2 \Delta q^2 + \left(\frac{\partial h}{\partial T_w}\right)^2 \Delta T_w^2 + \left(\frac{\partial h}{\partial T_{bulk}}\right)^2 \Delta T_{bulk}^2} \tag{3}$$

Thus the relative uncertainty can be computed by substituting Eq. (2) into Eq. (3), yielding

$$\frac{\Delta h}{h} = \sqrt{\left(\frac{\Delta q}{q}\right)^2 \Delta q^2 + \left(\frac{\Delta T_w}{T_w - T_{bulk}}\right)^2 + \left(\frac{\Delta T_{bulk}}{T_w - T_{bulk}}\right)^2} \tag{4}$$

where Δq, ΔT_w and ΔT_{bulk} are the uncertainties of heat flux, wall surface temperature and pool liquid temperature. The maximum uncertainty of h was obtained by a smaller surface temperature and a larger pool liquid temperature. Thus we achieved the maximum relative error of 8.52% for h. Table 2 shows the major physical properties of acetone at atmospheric pressure [14].

3. Results and discussion

3.1. Boiling heat transfer performance on various heater surfaces

Fig. 5 shows the boiling curves on the seven heater surfaces at three pool liquid temperatures of 38, 48 and 55 °C. According to Fig. 5, the seven heater surfaces can be divided into three types. The first type refers to the plain surface (TS#1) holding poorest heat transfer performance. The second type refers to the moderate enhanced heat transfer surfaces (TS#2 for open channel surface and TS#3 for thick uniform porous coating surface), and the third type is the significantly enhanced heat transfer surfaces which have 2-D and 3-D porous coatings with varied particle layer thicknesses (TS#4–7).

The boiling curves are intercrossed for the second type surfaces (TS#2 and 3). Fig. 5 marked the junction points. At the wall superheats smaller than those at the junction points, TS#3 (uniform porous coating surface) behaves better heat transfer performance than TS#2. This is because the porous surface provides a large amount of nucleation sites to enhance the nucleation heat transfer at small or moderate wall superheats (or heat fluxes). Inversely, when the wall superheats (or heat fluxes) are larger than those at the junction points, the open channel surface (TS#2) provides specific vapor escape channels to decrease the counterflow resistance between vapor and liquid phases, yielding better heat transfer performance. The junction points are shifted with varied pool liquid temperatures. For instance, the junction point occurred at ΔT_{sat} = 13 K with T_{bulk} = 38 °C, but appears at ΔT_{sat} = 18 K with T_{bulk} = 55 °C. The two heater surfaces had similar CHF values, but the wall superheats at CHFs are slightly different.

The third type heater surfaces (2-D surface of TS#4–6 and 3-D surface of TS#7) significantly enhance the pool boiling heat transfer. An important parameter influencing the performance is the pitch width for the 2-D porous coating surfaces. TS#4–6 have the pitch widths of 1.0, 1.6 and 2.0 mm respectively. The TS#5 surface, having the largest slope of the boiling curve, provides the best heat transfer performance among the three surfaces of TS#4, 5 and 6, indicating an optimal pitch width existed. This is because a small pitch width (w) generates sufficient capillary assisted liquid suction capability, but the flow path for vapor escape may be insufficient. On the other hand, a large pitch width supplies enough vapor escape but the liquid suction may be insufficient. Generally, the optimal pitch width depends on the balance between the liquid suction and vapor escape, yielding an optimal pitch width. The 3-D porous coating surface (TS#7) shows small difference of heat

Author's personal copy

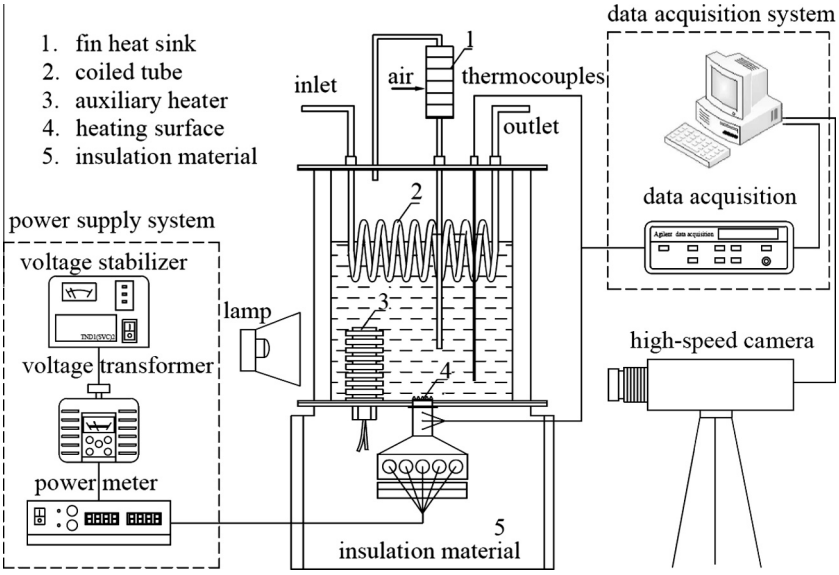

Fig. 4. The experimental setup.

Table 2
Physical properties of acetone at the atmosphere pressure.

T_{sat} (°C)	ρ_l (kg/m^3)	C_{pl} (J/kg K)	C_{pv} (J/kg K)	h_{lv} (kJ/kg)	σ (N/m)	μ_l (Pa s)	K_l (W/m K)
56.29	761.18	2302.5	1380.6	512.94	0.0192	0.000237	0.518

Where T_{sat} is the saturation temperature, ρ_l is the liquid density, C_{pl} and C_{pv} are the specific heat of liquid and vapor, h_{lv} is the latent heat of evaporation, σ is the surface tension, μ_l is the liquid viscosity, k_l is the thermal conductivity of liquid.

transfer performance with TS#4 (2-D surface with $w = 1.0$ mm), but TS#7 has much larger CHFs than TS#4.

3.2. Effect of pool liquid subcoolings on the heat transfer

Fig. 6a shows the heat transfer coefficients for the 3-D porous coating surface. The h–q curve can be divided into three regions. Region I refers to the nucleation heat transfer mechanism, with significantly steep slope of h–q curve. At a specific heat flux, a transition point clearly appears, beyond which the slope of the h–q curve significantly decreases until the maximum heat transfer coefficient. Region II refers to the region between the transition point of the h–q curve and the maximum h (see Fig. 6a with $T_{bulk} = 55$ °C). Region II is the region with the heat transfer process controlled by the balance between the liquid suction towards the porous surface and vapor escape into the pool liquid. At the maximum heat transfer coefficient, the liquid–vapor counterflow attains the best match between liquid suction and vapor release. At heat flux larger than that at the maximum point, the vapor release is so violent that the mass flow rate of liquid suction is not sufficient to compensate the consumed liquid by the vapor generation. Therefore, region III is a deteriorated heat transfer region until CHF was reached. There are no apparent transition points of h–q curve for subcooled boiling.

Fig. 6b shows the boiling curves for TS#7 with three pool liquid temperatures. It is seen that boiling curves were shifted to left (smaller wall superheat region) when liquid subcooling was introduced. Fig. 6b was used for comparison with other studies regarding the liquid subcooling effect. Another finding is that lower pool liquid temperatures also raise the critical heat fluxes, which will be discussed in Section 3.3.

It is well known that the main mechanism causing boiling heat transfer to have a much higher heat flux than free or forced convective heat transfer is due to an intense microconvection adjacent to the heater surface induced by the growing, departure, or collapsing of bubbles. The heat flux produced by the subcooling is dependent on ΔT_{sub} and bubble lifetime and average maximum bubble diameters, where $\Delta T_{sub} = T_{sat} - T_{bulk}$. Therefore, when the subcooling is introduced, the increase of subcooling produces two opposing effects. It increases the microconvection heat flux due to the increase of ΔT_{sub} and the decrease of bubble time. On the other hand, it reduces the average maximum bubble diameter and, therefore, decreases the microconvection heat flux. The net effect of subcooling on heat transfer depends on the relative influence of these opposing effects.

The Marangoni effect also appears during the pool boiling heat transfer. The liquid motion induced by surface tension variation, termed the Marangoni effect, and its contribution to boiling heat transfer has been an issue of much controversy. The classical boiling heat transfer theory considers its contribution to heat transfer to be insignificant in comparison with buoyancy induced convection. However, recent microgravity experiments have shown that although the boiling mechanism in a reduced gravity environment is different, the corresponding heat transfer rates are similar to those obtained under normal gravity conditions, raising questions about the validity of the assumption [15]. Petrovic et al. [15] performed an experimental investigation in which distilled water was gradually heated to boiling conditions on a copper heater surface at four different levels of subcooling. Photographic investigation of the bubbles appearing on the surface was carried out in support of the measurements. The results obtained indicate that Marangoni convection associated with the bubbles formed by the air dissolved in the water which emerged from solution when the water was heated sufficiently, significantly influenced the heat transfer rate in subcooled nucleate pool boiling. The authors developed a heat transfer model to explain the phenomena observed [15].

Author's personal copy

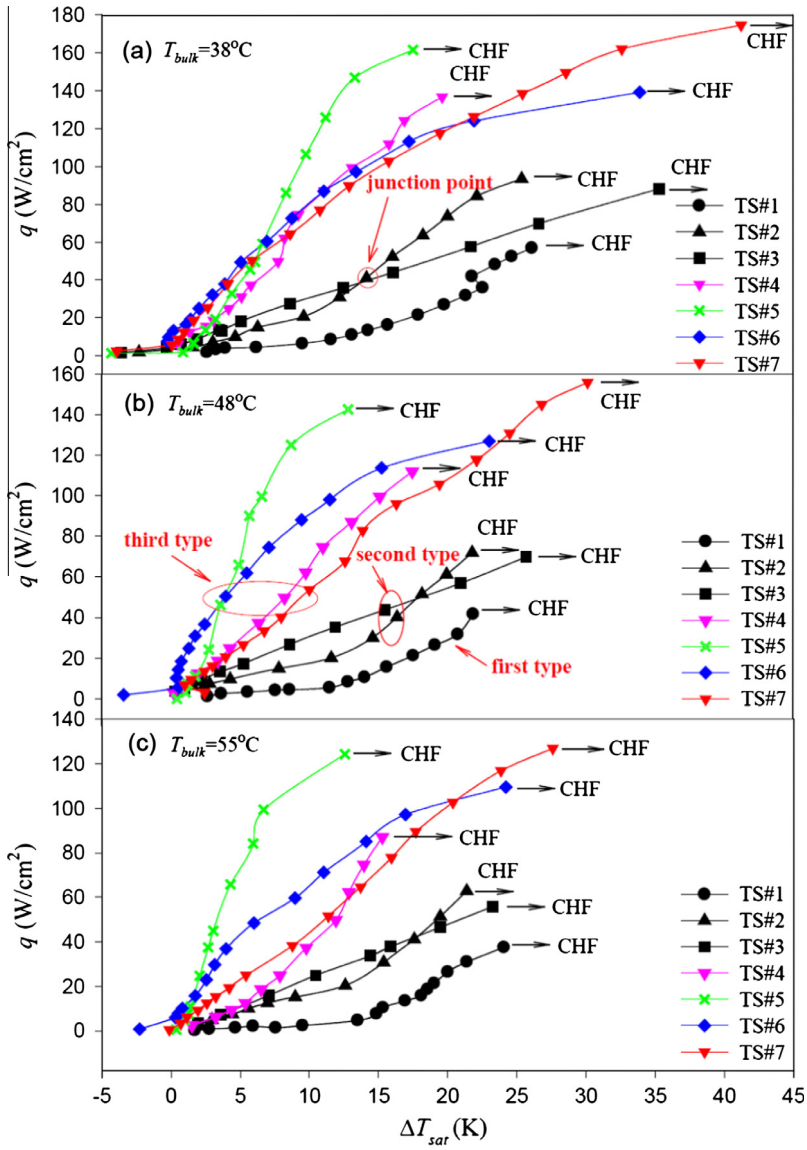

Fig. 5. Boiling curves for various heater surfaces.

Due to the opposing effects of liquid subcooling on the pool boiling, there are two major types of experimental findings existed in the literature. The first type refers to that boiling curves were shifted to smaller wall superheat region when liquid subcooling was introduced. Earlier studies by Lee and Singh [16] experimentally found that boiling curves were shifted to left (small wall superheat region) for pool boiling on stainless steel tube and platinum wire with increases in liquid subcoolings. Parker and El-Genk [17] and El-Genk and Parker [18] found that the nucleate pool boiling heat transfer could be enhanced with subcooling and CHF increased linearly with ΔT_{sub}.

Our experimental study of the pool boiling on varied-porous-coating-thickness surfaces belongs to the first type, i.e., boiling curves were shifted to smaller wall superheat region and CHF was increased with ΔT_{sub}. In addition to the available analysis on the opposing effects of subcooling above the heater surface, pool boiling with porous coating surface becomes more complicated. This is because the subcooled liquid may condense the vapor–liquid interface and increase the liquid suction capability within the porous structure.

The second type of pooling boiling states that the liquid subcooling level deteriorates the heat transfer, i.e., boiling curves were shifted to larger wall superheat region. An example case was demonstrated by Kim et al. [19], in which pool boiling on treated surfaces was investigated experimentally. Surface treatments were performed with sandpapers, building microstructures by etching, and micro-porous coating. The effect of liquid subcooling (0, 5, 10 K) on treated surfaces was reported.

3.3. Critical heat fluxes on various porous heater surfaces

The critical heat flux is a heat flux at which a small increment will yield a fast wall temperature rise until the heater surface is burned out. For this application, we monitor the wall temperature change rate. The heat flux is believed to appear when the wall temperature change rate attains 2 K/s. Table 3 shows the CHFs on various heater surfaces at the three pool liquid temperatures. The fourth column lists the ratios of CHF on the modified heater surface to that on the plain surface. Fig. 7 plotted the CHF values. The modified heater surfaces had larger CHFs than those on the plain surface. The open channel surface (TS#2) and the thick porous coating surface (TS#3) had similar CHF values, which are 1.5–1.7 times of those on the plain surface (TS#1). It is noted that the enhancement mechanisms of CHFs on two surfaces (TS#2 and 3)

Author's personal copy

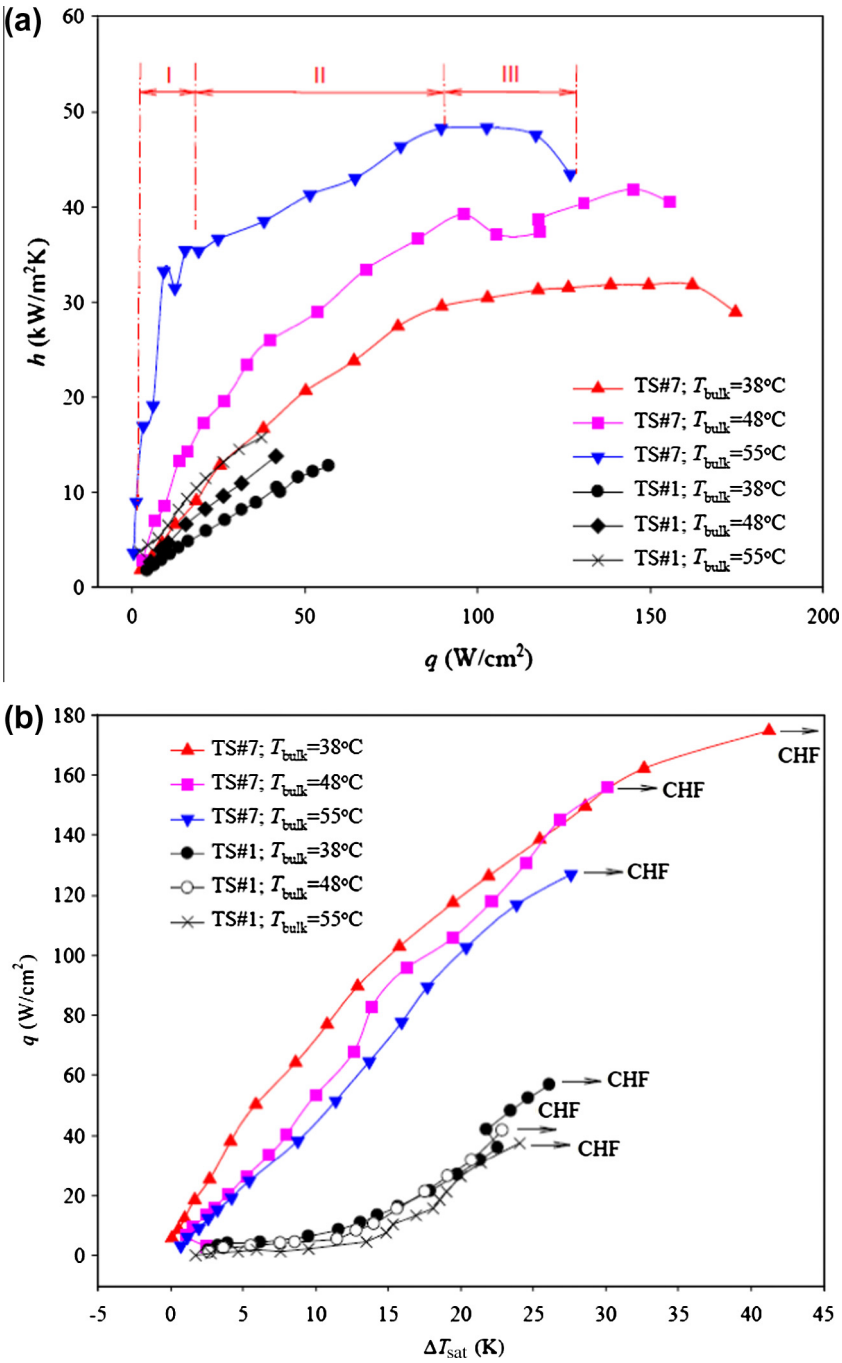

Fig. 6. Heat transfer coefficients and boiling curves on the 3-D porous coating surface (TS#7) and plain surface (TS#1).

are different. The open channel surface (TS#2) provides periodical vapor escape channel but the uniform porous coating surface (TS#3) provides strong capillary assisted liquid suction capability.

The CHFs on the 2-D and 3-D porous coating surfaces (TS#4–7) are 2.3–3.7 times of those on the plain surface (TS#1). The largest CHF ratio of 3.7 appears for the 3-D porous coating surface at the pool liquid temperature of 38 °C. The 3-D porous coating surface (TS#7) creates the largest CHFs among all of the modified heater surfaces. But the difference between the 3-D surface (TS#7) and 2-D surface with $w = 1.6$ mm (TS#5) is not too much. Besides, the effect of pool liquid temperatures on CHFs cannot be ignored (Table 3 and Fig. 7). For TS#7, CHF was 174.69 W/cm^2 at $T_{bulk} = 38$ °C, but decreased to 126.87 W/cm^2 at $T_{bulk} = 55$ °C. Other heater surfaces had similar trend with TS#7 regarding the pool liquid temperature effect.

Liter and Kaviany [8] developed the critical heat flux as a function of λ_m (modulation wavelength) based on the Zuber's hydrodynamic stability theory. Zuber developed a theoretical model for q_{CHF} based on the idealized hydrodynamics of a liquid–vapor interface system above the surface in pool boiling considering the ability to supply liquid to the surface where the vapor escapes. Based on the Zuber's hydrodynamic stability theory, the portion of the cross-section flow area for vapor escape on the heated area and the critical Rayleigh–Taylor wavelength are crucial to determine q_{CHF}. It was hypothesized that the heated area is divided into $A_b = A_v + A_l$, where A_v is the area where the vapor escapes and A_l is the area for liquid covers. The cylindrical vapor channel area of $A_v = \pi R_v^2$, where the radius $R_v = a\lambda_b$, a is ratio of R_v/λ_b, and λ_b is the length scale, i.e., $A_b = \lambda_b^2$. The final relation of q_{CHF} with other parameters is

Author's personal copy

Table 3
The measured critical heat fluxes (CHF) on various heater surfaces at three pool liquid temperatures.

Heater surface	T_{bulk} (°C)	CHF (W/cm^2)	CHF/CHF$_{plain}$
TS#1	38	56.94	1.0
	48	41.66	1.0
	55	37.50	1.0
TS#2	38	93.49	1.6
	48	71.96	1.7
	55	62.82	1.7
TS#3	38	88.19	1.5
	48	69.86	1.7
	55	55.88	1.5
TS#4	38	136.76	2.4
	48	111.89	2.7
	55	87.03	2.3
TS#5	38	161.67	2.8
	48	142.52	3.4
	55	124.32	3.3
TS#6	38	135.27	2.4
	48	126.87	3.0
	55	109.50	2.9
TS#7	38	174.69	3.1
	48	155.77	3.7
	55	126.87	3.4

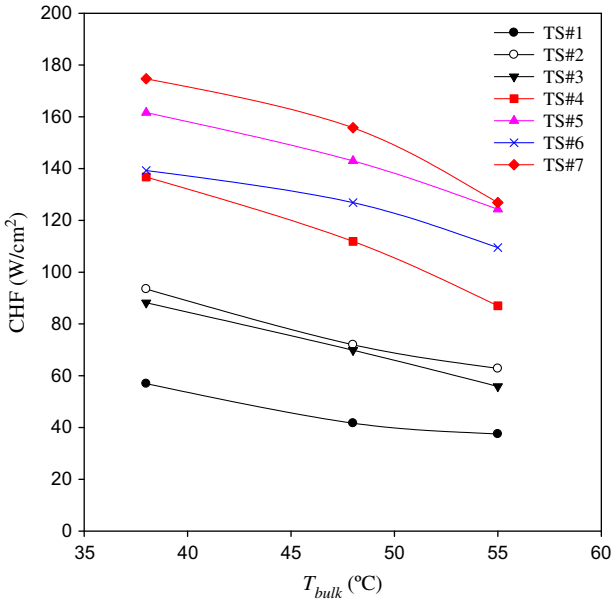

Fig. 7. Critical heat fluxes (CHFs) on various heater surfaces.

$$\frac{q_{CHF}}{\pi\rho_v^{1/2}\Delta h_{lv}\left[(\rho_l-\rho_v)\sigma g\right]^{1/4}} = \frac{3\left[\frac{\sigma}{(\rho_l-\rho_v)g}\right]^{1/4}}{\lambda_m^{1/2}} \quad (5)$$

Eq. (5) indicates that q_{CHF} is inversely proportional to the modulation wavelength $\lambda_m^{1/2}$. Eq. (5) does not relate q_{CHF} to any porous structure parameter such as particle diameter (d_p) and porosity (ε). Min et al. [9] compared their own data as well as data of Liter and Kaviany [8] with predictions by Eq. (5). It was found that Eq. (5) matched the experimental data. However, the 3-D modulated surface (#262 with λ_m = 0.93 mm in Min et al. [9]) was against the predicted trend of CHF given by Eq. (5).

Comparing TS#4, 5 and 6 with pitch widths of 1.0, 1.6 and 2.0 mm respectively in this study, CHFs for TS#5 are largest among the three heater surfaces, indicating an optimal modulation wavelength of 1.6 mm for TS#5. This experimental finding did not support the predicted trend by Eq. (5). Physically, a non-uniform porous coating surface with very small modulation wavelength, should approach the CHF of a uniform porous coating surface, which had much smaller CHFs. This trend cannot be predicted by Eq. (5). The Zuber's hydrodynamic stability theory should be further modified to consider the modulation wavelength effect and other porous parameters.

3.4. High speed visualization of boiling patterns on various heater surfaces

Fig. 8 shows the boiling patterns for the 2-D porous coating surface (TS#5) at T_{bulk} = 38 °C. The photos are provided for different heat fluxes. Very tiny bubbles are escaping from the valley groove at q_a = 6.67 W/cm^2, which can be identified as the ONB (onset of boiling). When heat flux is increased beyond that at ONB, tiny bubbles are coalescence to form large bubbles, which are continuously escaping to the pool liquid (see photos at q_b = 32.96 W/cm^2 and q_c = 59.21 W/cm^2 in Fig. 8). The merged bubbles, however, are smaller than the entire heater size. At these small or moderate heat fluxes, liquid supply towards the porous surface is sufficient due to the existed gaps among isolated bubbles. This bubble pattern is called the continuously-isolated-bubble-escape pattern.

With further increases of heat fluxes such as at q_d = 106.56 W/cm^2 and q_e = 147.01 W/cm^2, the merged bubble size is almost equivalent to the plain heater size. The large bubble escape displays the periodic behavior. For instance, for q_d = 106.56 W/cm^2 at t = 36.0 ms, the large bubble is separating from the vapor blanket on the heater surface and releasing into the pool liquid. Shortly after the merged bubble separated from the heater surface, the bubbles on the heater surface are quickly growing, coalescence and departure again. This process is repeated periodically. The liquid supply towards the porous heater surface can be performed during the short stage of large bubble separating and releasing. Increasing the heat flux yields the longer cycle period to cause more difficulty for liquid supply. This bubble pattern at larger heat fluxes is called the periodically-large-bubble-escape pattern.

Saturated pool boiling heat transfer on the 3-D porous surface (TS#7) behaves three regions: region I for the nucleation heat transfer, region II for the balance of liquid supply and vapor escape, and region III for the deteriorated heat transfer. Fig. 9 illustrates the boiling patterns for the three regions. Corresponding to the region I heat transfer, miniature bubbles departure from the porous surface into the pool liquid, liquid supply is sufficient. At small heat flux of q_a = 1.24 W/cm^2, miniature bubbles are escaping from specific location of the valley of the porous stacks, forming a miniature bubble train. With increase of heat fluxes, many bubbles appear and continuously escape into the pool liquid. The bubble size and population density are increased when heat flux is raised. The region I (nucleation heat transfer) corresponds to the continuously-isolated-bubble-escape pattern (see images at q_b = 3.33 and q_c = 6.14 W/cm^2).

The region II heat transfer obeys the periodically-large-bubble-escape pattern (see photos of q at point d–f, and g in Fig. 9). Large merged bubble, whose size is equivalent to the whole plain heater size, is periodically escaping into the pool liquid. After the large bubble successfully departures from the heater surface, the growing vapor bubble on the heater surface forms a hollow area at the heater center. This hollow region provides the opportunity for the liquid supply. The escaping vapor is more likely foam-type bubbles.

Fig. 10 compares different boiling patterns on various heater surfaces at a same heat flux of q = 37.49 W/cm^2. The plain heater surface (TS#1) shows the mushroom bubble departure pattern (see photo a). There is a vapor blanket layer underneath the

Author's personal copy

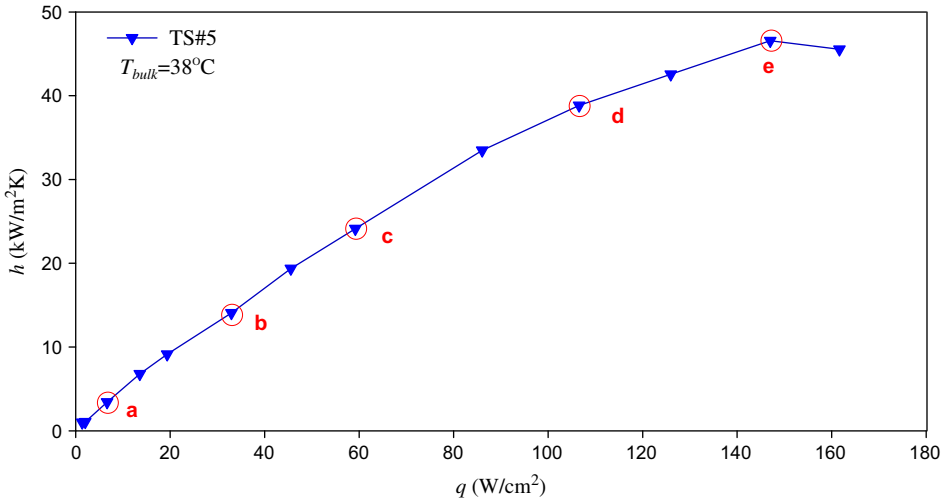

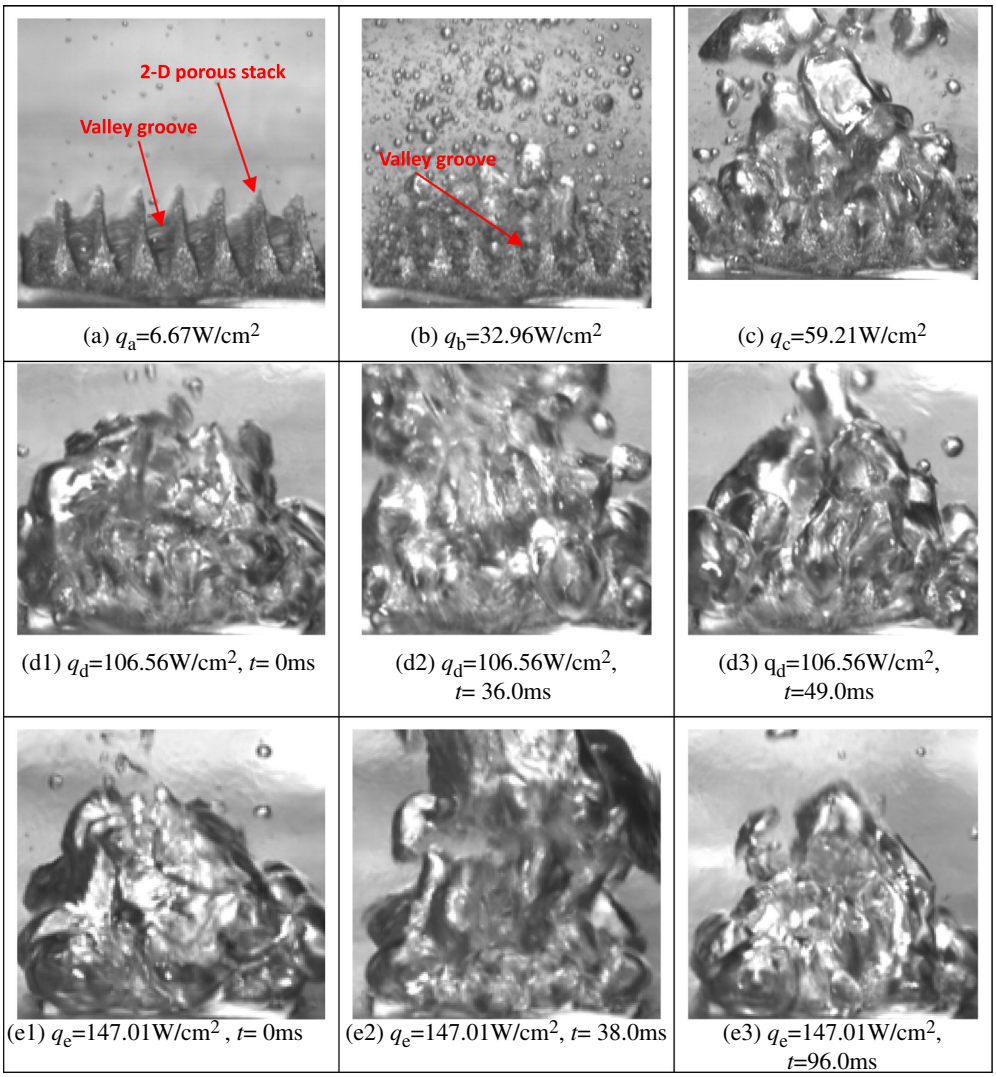

(a) q_a=6.67W/cm^2 (b) q_b=32.96W/cm^2 (c) q_c=59.21W/cm^2

(d1) q_d=106.56W/cm^2, t= 0ms (d2) q_d=106.56W/cm^2, t= 36.0ms (d3) q_d=106.56W/cm^2, t=49.0ms

(e1) q_e=147.01W/cm^2 , t= 0ms (e2) q_e=147.01W/cm^2, t= 38.0ms (e3) q_e=147.01W/cm^2, t=96.0ms

Fig. 8. Boiling visualization on the 2-D porous coating surface (TS#5, image (a) for boiling incipience pattern, images (b) and (c) for continuous-bubble-escape pattern, images (d) and (e) for periodical-large-bubble-escape patterns at different time).

mushroom bubble, hindering the liquid supply towards the heater surface. This condition approaches the critical heat flux. The thick uniform porous coating surface (TS#3) does not have significant difference with the plain surface (TS#1) regarding the bubble pattern at $q = 37.49$ W/cm^2 (see photo b). For the 3-D surface (TS#7) and 2-D surface (TS#5), even though the bubbles are covered on the heater surface, these bubbles are fragmented to provide the chance for liquid supply (see photos c and d). This

Author's personal copy

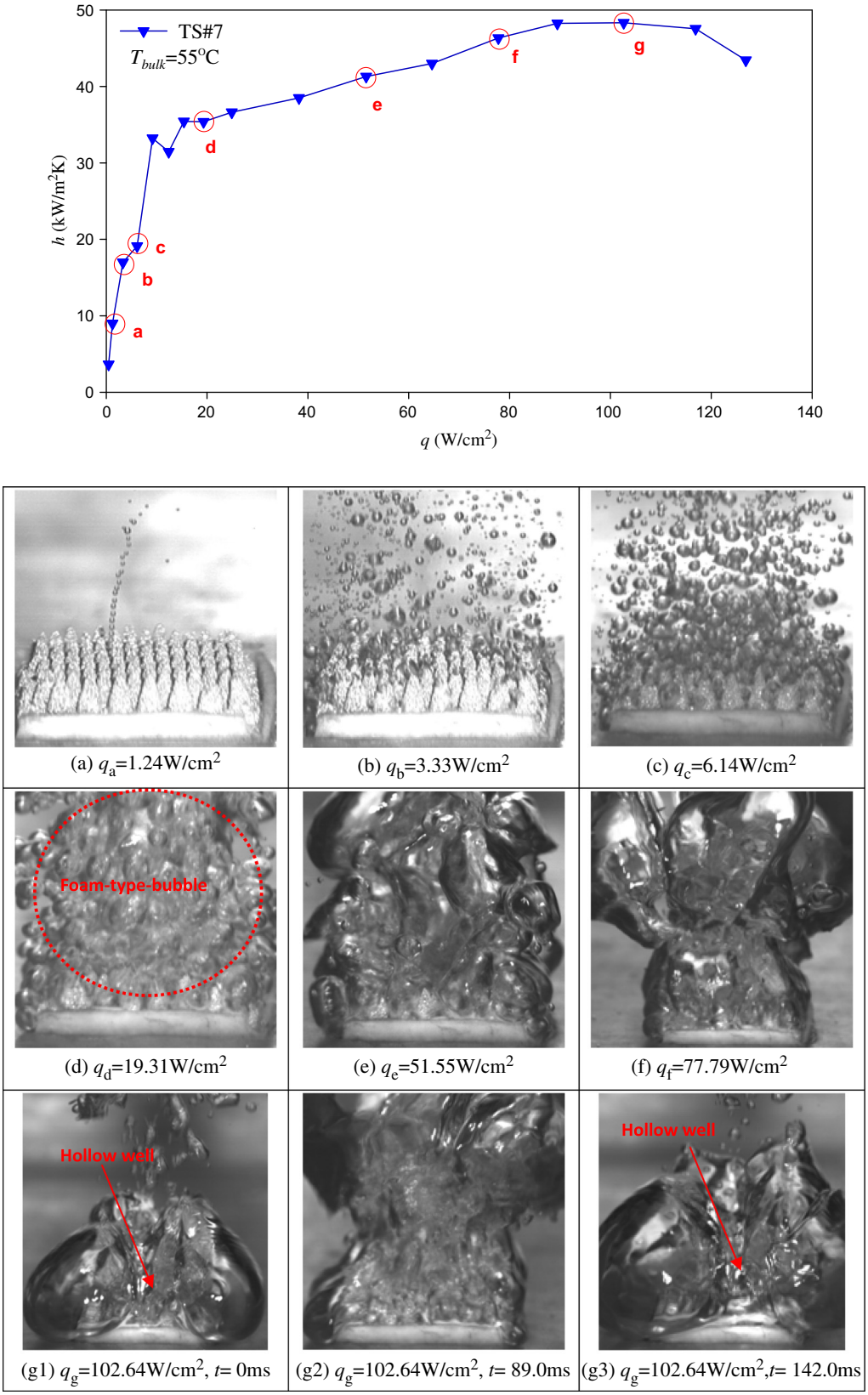

Fig. 9. Boiling visualization on the 3-D coating surface (TS#7, T_{bulk} = 55 °C, image (a) for boiling incipience pattern, images (b–f) for continuous-bubble-escape patterns, image (g) for high heat flux pattern at different time).

explains the reason why the 2-D and 3-D surfaces had better heat transfer performance than the plain surface (TS#1) and thick uniform porous coating surface (TS#3).

Fig. 11 shows the bubble patterns at the ONB on various heater surfaces. The boiling incipience for the plain heater surface (TS#1) appears at the wall superheat of about 10 K and wall heat flux of

Author's personal copy

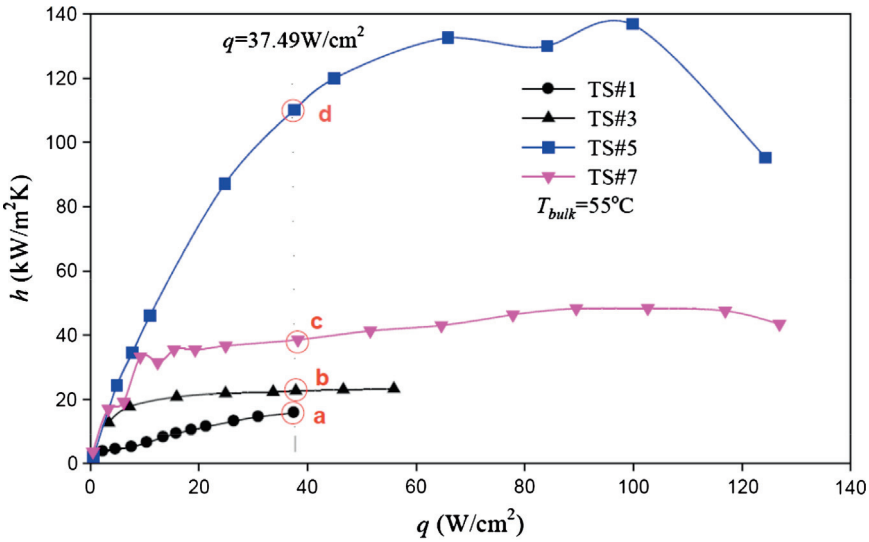

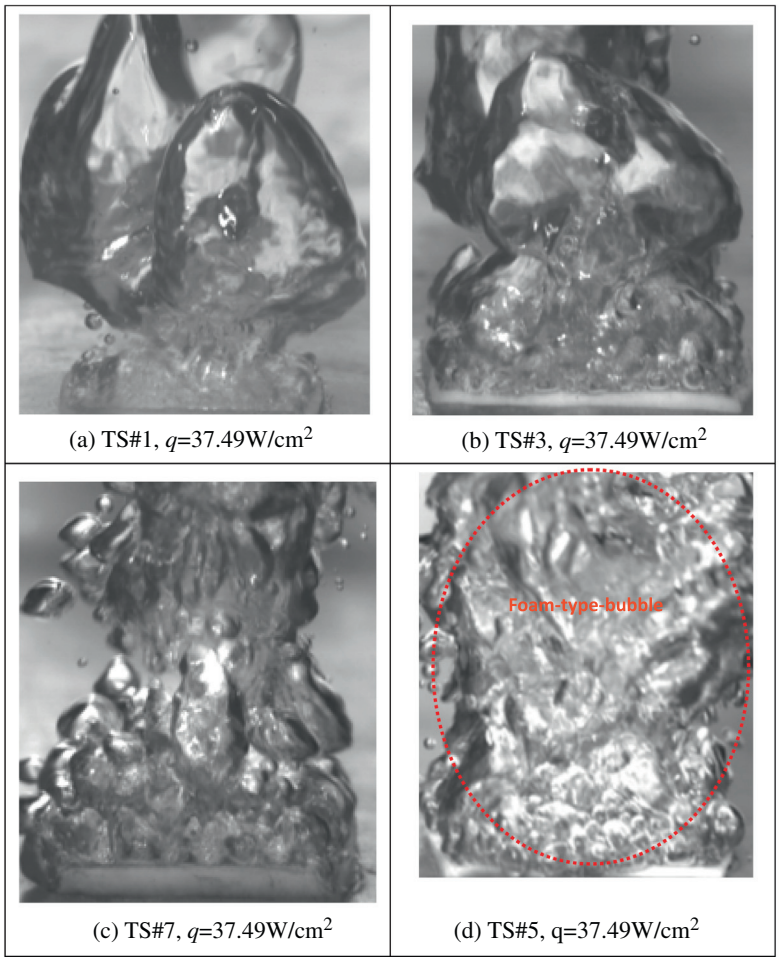

(a) TS#1, q=37.49W/cm^2 (b) TS#3, q=37.49W/cm^2

(c) TS#7, q=37.49W/cm^2 (d) TS#5, q=37.49W/cm^2

Fig. 10. Boiling visualization on various heater surfaces at a same heat flux (T_{bulk} = 55 °C).

4.79 W/cm^2 (see photo a). The open channel surface (TS#2) decreased the wall superheat to 3 K due to the extended fin area (see photo b). The 2-D and 3-D porous surfaces have the wall superheats of about 1 K at the ONB due to the significantly increased nucleation sites, in which TS#3 and 7 have large amount of miniature bubbles continuously escaping into the pool liquid (see images at d–f in Fig. 11).

Finally, we demonstrate the bubble patterns at extremely high heat fluxes, approaching CHFs. The bubble patterns on all the heater surfaces display the periodic behavior. However, they are quite different due to different heater surface structures. Fig. 12a shows the bubble patterns on the uniform coating surface (TS#3). The whole heater surface is covered by a vapor blanket. The escape of large mushroom bubble still ensures the completeness of the vapor

Author's personal copy

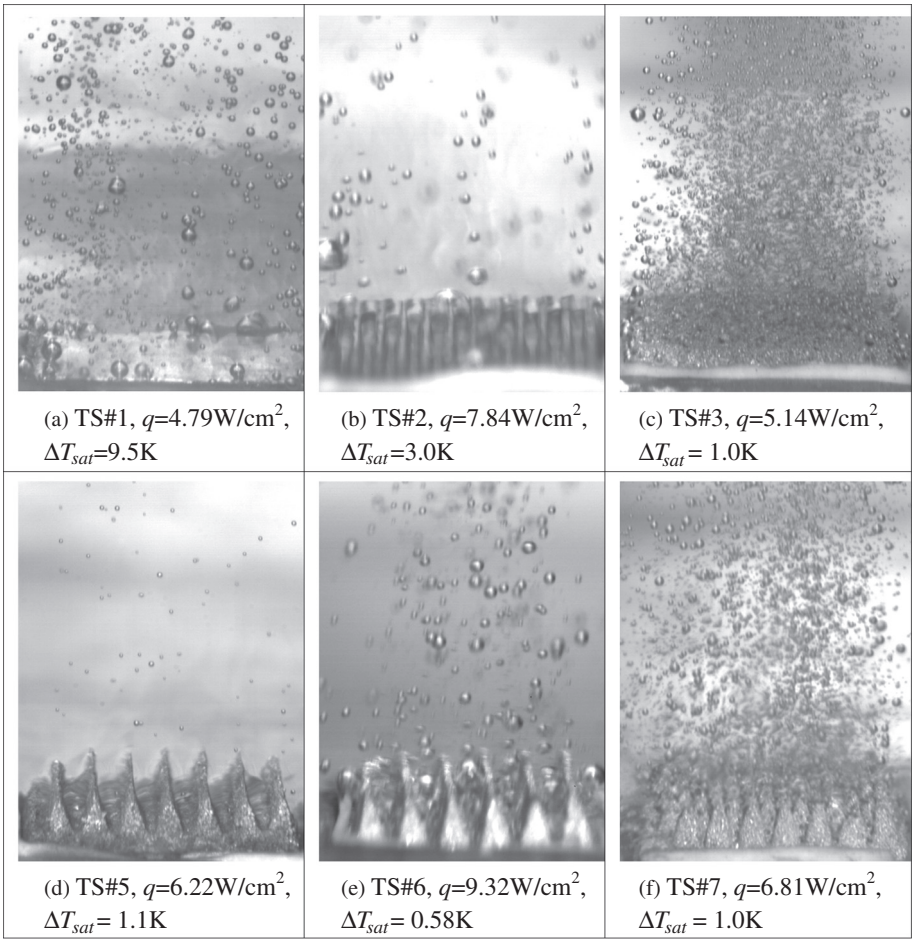

Fig. 11. Boiling visualization at the ONB (onset of boiling) with T_{bulk} = 48 °C.

blanket. Such condition is dangerous because there is almost no liquid supply towards the porous heater surface, approaching CHF. For the 2-D and 3-D surfaces (TS#5 and 7, see Fig. 12b and c), a hollow well is found after the large bubble separated from the heater surface, leaving a hollow region for the liquid supply towards the porous heater surface. In addition to the hollow well, the 3-D porous stacks can be found to be temporarily exposed in the liquid. The existence of hollow well at the heater center is the reason to have higher critical heat fluxes for the 2-D porous heater surface (TS#5). The existence of hollow well and the porous stacks exposed in liquid are the reason to have significantly high critical heat fluxes for the 3-D porous coating surface (TS#7).

4. Conclusions

We performed the pool boiling heat transfer experiments on seven heater surfaces using acetone as the working fluid at atmospheric pressure. The following conclusions can be made.

- The heater surfaces can be divided into three types. The first, second and third types refer to the poor heat transfer surface for plain surface, the moderate enhanced heat transfer surfaces for open channel surface and uniform porous coating surface, and the significantly enhanced heat transfer surfaces having 2-D and 3-D porous coatings.
- The boiling curves are intercrossed for the open channel surface and uniform porous coating surface. With heat fluxes smaller than that at the junction point, the uniform porous coating surface behaves better heat transfer performance due to the enhanced nucleation heat transfer. When heat fluxes are beyond that at the junction point, the open channel surface shows the better heat transfer performance due to the vapor escape channels provided.
- The 2-D porous coating surface with the pitch width of 1.6 mm (TS#5) yields the best heat transfer performance and largest critical heat fluxes among the three 2-D surfaces. The Zuber's hydrodynamic stability theory should be further improved to consider the flow and heat transfer process within the porous stacks and vapor channels.
- The 3-D porous coating surface (TS#7) had the largest critical heat fluxes among the seven heater surfaces. The CHF for TS#7 can be 3.7 times of that for the plain surface.
- Boiling curves are shifted to smaller wall superheat region and critical heat fluxes are increased with increases in pool liquid subcoolings on porous coating surfaces. This finding is consistent with those reported in Refs. [16–18], but against that reported in Ref. [19].
- The 2-D and 3-D porous coating surfaces had two distinct bubble patterns: continuously-isolated-bubble-escape pattern at small or moderate heat fluxes, and the periodically-large-bubble-escape pattern at large heat fluxes. The bubbles are more likely foam-type, accounting for the improved heat transfer due to the liquid supply.
- The hollow well at the heater center after the large bubble escape is used as the liquid supply duct, being responsible for the increased critical heat fluxes for 2-D surfaces. The hollow

Author's personal copy

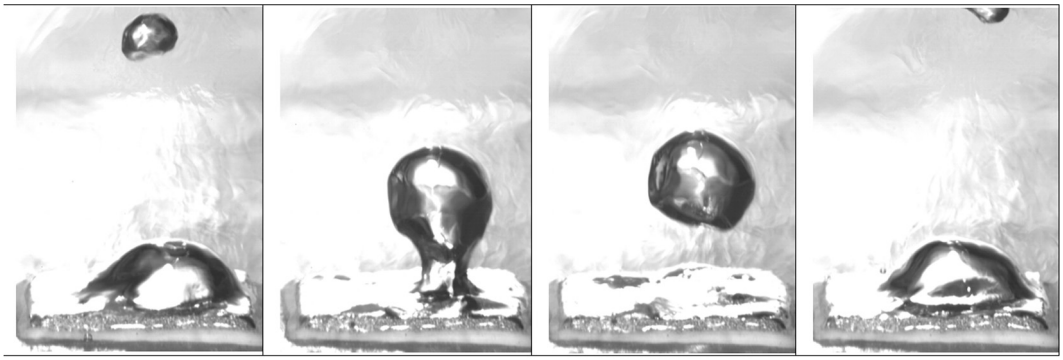

0ms 29.0ms 34.0ms 77.0ms

(a) TS#3 (q=88.19 W/cm^2)

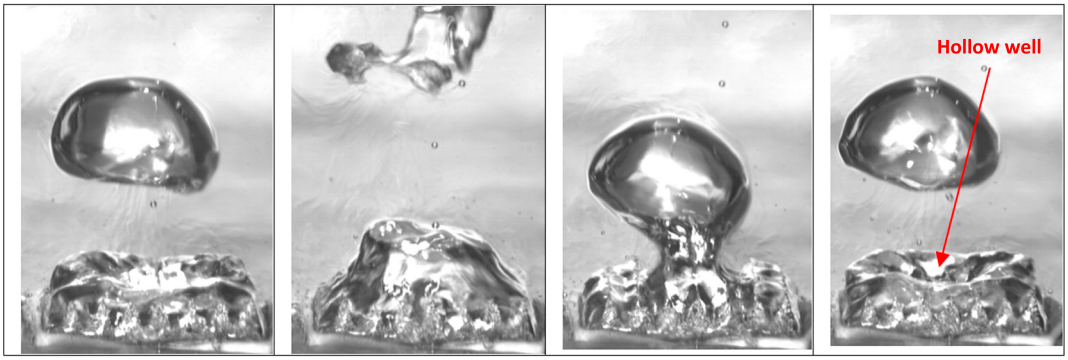

0ms 27.0ms 56.0ms 71.0ms

(b) TS#5 (q=165.67 W/cm^2)

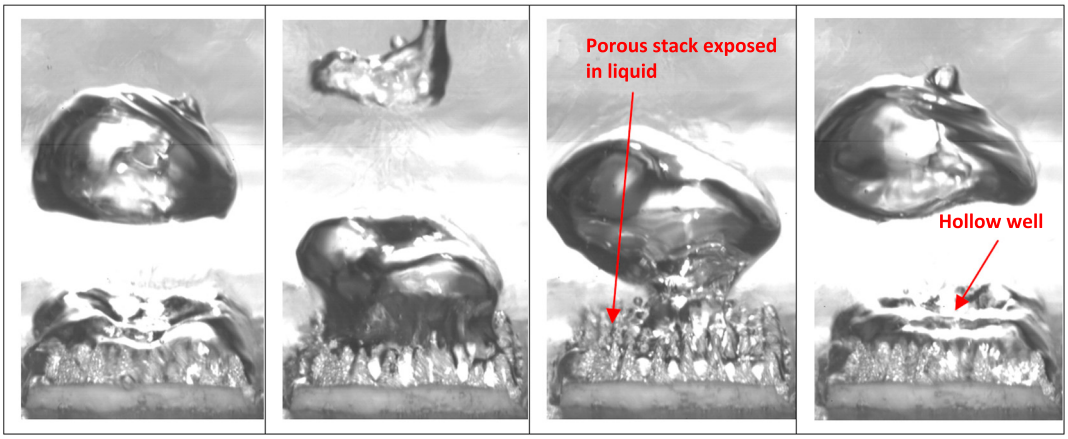

0ms 29.0ms 50.0ms 66.0ms

(c) TS#7 (q=174.69 W/cm^2)

Fig. 12. Boiling visualization on various heater surfaces at high heat fluxes approaching CHF (T_{bulk} = 38 °C).

well and the porous stacks exposed in liquid are helpful for the liquid supply, explaining the largest critical heat fluxes for 3-D porous coating surface.

Acknowledgements

This work was supported by the joint funding from Natural Science Foundation of China and Guangdong Province (U1034004), the Natural Science Foundation of China of International Cooperation Project (51210011), Natural Science Foundation of China (51276061) and the Beijing Science and Technology Program (Z111109055311097).

References

[1] Y.Y. Jiang, W.C. Wang, D. Wang, B.X. Wang, Boiling heat transfer on machined porous surfaces with structural optimization, International Journal of Heat and Mass Transfer 44 (2) (2000) 443–456.
[2] J.J. Wei, H. Honda, Effects of fin geometry on boiling heat transfer from silicon chips with micro-pin-fins immersed in FC-72, International Journal of Heat and Mass Transfer 46 (2003) 4059–4070.
[3] G.S. Hwang, M. Kaviany, Critical heat flux in thin, uniform particle coatings, International Journal of Heat and Mass Transfer 49 (2006) 844–849.

Author's personal copy

[4] R.L. Webb, Principles of Enhanced Heat Transfer, John Wiley & Sons, New York, 1992.
[5] E. Meléndez, R. Reyes, The pool boiling heat transfer enhancement from experiments with binary mixtures and porous heating covers, Experimental Thermal and Fluid Science 30 (2006) 185–192.
[6] J.Y. Chang, S.M. You, Enhanced boiling heat transfer from micro-porous surfaces: effects of a coating composition and method, International Journal of Heat and Mass Transfer 40 (18) (1997) 4449–4460.
[7] W. Wu, J.H. Du, X.J. Hu, B.X. Wang, Pool boiling heat transfer and simplified one-dimensional model for prediction on coated porous surfaces with vapor channels, International Journal of Heat and Mass Transfer 45 (5) (2002) 1117–1125.
[8] S.G. Liter, M. Kaviany, Pool boiling CHF enhancement by modulated porous-layer coating: theory and experiment, International Journal of Heat and Mass Transfer 44 (2001) 4287–4311.
[9] D.H. Min, G.S. Hwang, Y. Usta, O.N. Cora, M. Koc, M. Kaviany, 2-D and 3-D modulated porous coatings for enhanced pool boiling, International Journal of Heat and Mass Transfer 52 (2009) 2607–2613.
[10] T. Semenic, I. Catton, Experimental study of biporous wicks for high heat flux applications, International Journal of Heat and Mass Transfer 52 (2009) 5113–5121.
[11] F.C. Lin, B.H. Liu, C.T. Huang, Y.M. Chen, Evaporative heat transfer model of a loop heat pipe with bidisperse wick structure, International Journal of Heat and Mass Transfer 54 (2011) 4621–4629.
[12] N. Zuber, Hydrodynamic aspects of boiling heat transfer AECU-4439, physics and mathematics, US Atomic Energy Commission (1959) 1–196.
[13] J.L. Xu, X.B. Ji, W. Zhang, G.H. Liu, Pool boiling heat transfer of ultra-light copper foam with open cells, International Journal of Multiphase Flow 34 (2008) 1008–1022.
[14] C.L. Yaws, Chemical Properties Handbook, Mcgraw-Hill, New York, 1999.
[15] S. Petrovic, T. Robinson, R.L. Judd, Marangoni heat transfer in subcooled nucleate pool boiling, International Journal of Heat and Mass Transfer 47 (2004) 5115–5128.
[16] L. Lee, B.N. Singh, The influence of subcooling on nucleate pool boiling heat transfer, Letters in Heat and Mass Transfer 2 (1975) 315–324.
[17] J.L. Parker, M.S. El-Genk, Enhanced saturation and subcooled boiling of FC-72 dielectric liquid, International Journal of Heat and Mass Transfer 48 (2005) 3736–3752.
[18] M.S. El-Genk, J.L. Parker, Enhanced boiling of HFE-7100 dielectric liquid on porous graphite, Energy Conversion and Management 46 (2005) 2455–2481.
[19] Y.H. Kim, K.J. Lee, D. Han, Pool boiling enhancement with surface treatments, Heat and Mass Transfer 45 (2008) 55–60.